Theory and experiment on laser-enabled inner-valence Auger decay of rare-gas atoms

X. M. Tong,[1,2,*] P. Ranitovic,[3] C. W. Hogle,[3] M. M. Murnane,[3] H. C. Kapteyn,[3] and N. Toshima[1]

[1]*Institute of Materials Science, Graduate School of Pure and Applied Sciences, University of Tsukuba, 1-1-1 Tennodai, Tsukuba, Ibaraki 305-8573, Japan*

[2]*Center for Computational Sciences, University of Tsukuba, 1-1-1 Tennodai, Tsukuba, Ibaraki 305-8577, Japan*

[3]*JILA and Department of Physics, University of Colorado and NIST, Boulder, Colorado 80309-0440, USA*

(Received 5 May 2011; published 11 July 2011)

In rare-gas atoms, an inner-valence shell ns hole cannot be filled by Auger decay because of an energy deficiency. We show theoretically and experimentally that by adding a moderately intense infrared laser, Auger decay is possible with decay rates increasing dramatically for laser intensities $\geqslant 10^{13}$ W/cm^2. For Xe atoms, the simulated laser-enabled Auger decay yields are comparable with the experimental one, while for Ar atoms, the simulated ones are much smaller. We attribute the discrepancies to screening effects of the photoelectron. Laser-enabled Auger decay is of fundamental importance for understanding attosecond science, and is also important for experimental applications in ultrafast atomic, molecular, and materials dynamics using x rays. More importantly it may provide a way to control the Auger decay time and selectively break chemical bonds of molecules using a control infrared laser field.

DOI: 10.1103/PhysRevA.84.013405 PACS number(s): 32.80.Hd, 32.80.Qk, 42.65.Re

I. INTRODUCTION

When an inner-shell vacancy is created in atoms or molecules, the inner-shell core hole can be filled by another electron either through radiative decay or Auger decay. The ejected electron in Auger decay encodes atomic or molecular information, which can be used to diagnose the constituents of materials. Due to rapid advances in technology, it has become possible to create an inner-shell core hole using attosecond extreme ultraviolet (XUV) pulses and to manipulate the photoelectron or Auger electron using an ultrafast infrared (IR) laser. In such a laser-assisted process, a system is simultaneously irradiated by attosecond XUV pulses and laser beams. Characteristic sidebands appear surrounding the photoemission and Auger peaks, corresponding to simultaneous absorption and emission of laser photons. The magnitude and shape of these sidebands change as a function of the time delay between the attosecond XUV and laser pulses, encoding information about the XUV pulse duration and underlying electron dynamics. In recent years, laser-assisted photoemission [1,2] and laser-assisted Auger decay have been used to characterize ultrafast XUV pulses, to study electron-electron correlations in atoms and molecules [3], and to measure core-hole lifetimes of atoms [4–10] or of adsorbates on surfaces [11]. However, in all of those studies, laser-assisted Auger decay represented a means by which an existing Auger decay channel could be modified and exploited.

In a recent experiment [12], short XUV and IR pulses were used to doubly ionize Ar in a time-resolved manner. A 42-eV XUV pulse was used to populate Rydberg states of Ar^+, just below the double-ionization (DI) threshold. In the presence of a moderately intense IR pulse, several DI pathways were discussed: IR-induced DI of the XUV-created Ar^{+*} and Ar^{**} states, and laser-enabled Auger decay (LEAD). The double ionization of Ar through the LEAD process occurs when the XUV photon creates a $3s$ inner-valence hole in the presence of a moderately intense laser field. Without the IR field, the $3s$ hole is filled by a $3p$ electron, radiatively relaxing on a nanosecond time scale. In the presence of an IR field, the $3s$ hole can be filled by a $3p$ electron on a femtosecond time scale though the LEAD process, where a second $3p$ electron is ejected into an Ar^{+*} Rydberg orbit, or is promoted into the double-ionization continuum. The LEAD double-ionization channel opens up if the laser intensities are high enough so that the atomic ions can absorb enough energy through multiphoton processes to bridge the gap between the DI threshold and the $3p \rightarrow 3s$ energy difference as depicted in Fig. 1. In the case of Ar, this energy is 14.08 eV, which is smaller than the ionization potential of Ar atoms. It was shown that even a moderate intensity of 10^{13} W/cm^2 can doubly ionize Ar with a rate higher than the rate of the $3p \rightarrow 3s$ radiative decay.

In this paper we expand the theoretical calculations to several other rare-gas atoms and show interesting experimental data. We organize this paper as follows: first we derive a general theory to describe the LEAD process, then we calculate the intensity-dependent LEAD rates for Xe, Kr, Ar, and Ne atoms, and finally we present the experimental single- and double-ionization yields of Xe and Ar atoms by a 36-eV XUV source with a moderate IR laser as a function of the femtosecond and attosecond time delays between the two pulses. Some of the observations can be explained by the LEAD process.

II. THEORETICAL METHODS

Figure 1 illustrates the LEAD process. Assuming that the wave functions of the atomic ion where an inner-valence hole ($N-1$ electron system), the doubly ionized ion core ($N-2$ electron system), and the Auger electron are $\Psi_h(N-1)$, $\Psi_c(N-2)$, and ψ_a with the corresponding Hamiltonians $H_h(N-1)$, $H_c(N-2)$, and h_a, respectively, we write the time evolution of the Auger electron wave function as (atomic

*tong@ims.tsukuba.ac.jp

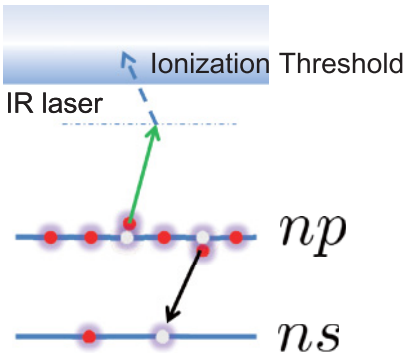

FIG. 1. (Color online) Schematic diagram of IR-enabled Auger decay in a rare-gas atom.

units $\hbar = m = e = 1$ are used through the paper unless stated otherwise)

$$\psi_a(\mathbf{r},t) = -i\int_{-\infty}^{t} e^{-i\int_{\tau}^{t} h_a(t')\,dt'} e^{-i(E_h-E_c)\tau} F(\mathbf{r})\,d\tau, \quad (1)$$

with

$$F(\mathbf{r}) = \langle \Psi_c(N-2)|V_{\rm res}(\tau)|\Psi_h(N-1)\rangle, \quad (2)$$

and $V_{\rm res}(\tau) = H_c(N-2) + h_a(\tau) - H_h(N-1)$. Here E_h and E_c are the energies of the $\Psi_h(N-1)$ and $\Psi_c(N-2)$ states, respectively. To derive the above equation, we assume that the IR laser only affects the Auger electron having the occupied orbitals in $\Psi_h(N-1)$ and $\Psi_c(N-2)$ unperturbed. Since the Auger process is a two-electron process, the electron-laser field interaction does not appear in Eq. (2). Thus, $F(\mathbf{r})$ can be evaluated as

$$F(\mathbf{r}) = \sum_{i=1}^{N-2}\langle \Psi_c(N-2)|\frac{1}{|\mathbf{r}-\mathbf{r}_i|}|\Psi_h(N-1)\rangle. \quad (3)$$

The Hamiltonian of the Auger electron in an IR field is written as

$$h_a(t) = -\frac{\nabla^2}{2} + V_{\rm eff}(r) - zE(t), \quad (4)$$

where $V_{\rm eff}(r)$ is the model potential [13] of the atomic ions, z the electron coordinate along the IR polarization direction, and $E(t)$ the IR field strength. For rare-gas atoms (Ne, Ar, Kr, or Xe), $|\Psi_h(N-1)\rangle$ stands for $|nsnp^6\ ^2S\rangle$, which can be recast as [14]

$$\begin{aligned}|\Psi_h(N-1)\rangle = &\frac{1}{\sqrt{15}}|ns(np^4\ ^1S)np^2\ ^2S\rangle \\ &+\frac{1}{\sqrt{3}}|ns(np^4\ ^1D)np^2\ ^2S\rangle \\ &+\sqrt{\frac{3}{5}}|ns(np^4\ ^3P)np^2\ ^2S\rangle. \end{aligned} \quad (5)$$

$|\Psi_c(N-2)\rangle$ is $|ns^2np^4\ ^1S\rangle$ or $|ns^2np^4\ ^1D\rangle$ where n is the principal quantum number of the highest occupied orbital. The last term in Eq. (5) does not contribute to the LEAD due to the conservation of angular momentum. The final doubly charged ions created by the LEAD can be in the ^1S (the upper limit is 1/15) or ^1D (the upper limit is 1/3) states, limiting the total double-ionization yield to be 40% of the hole population.

Defining a radial function $f(r)$ as

$$f(r) = \int_0^{\infty} R_{ns}(r_1)\frac{r_<}{r_>^2}R_{np}(r_1)R_{np}(r)r_1^2\,dr_1, \quad (6)$$

where $r_<$ ($r_>$) stands for the smaller (larger) one of the r and r_1, and R_{ns} and R_{np} are the radial wave functions of the ns and np states, we obtain

$$F(\mathbf{r}) = \begin{cases} -\frac{1}{\sqrt{3}}f(r)Y_{00}(\hat{\mathbf{r}}) & \text{for } ^1S, \\ -\sqrt{\frac{2}{15}}f(r)Y_{2M}(\hat{\mathbf{r}}) & \text{for } ^1D. \end{cases} \quad (7)$$

^1S (^1D) stands for the final state of the doubly ionized species. Using the expression for $F(\mathbf{r})$ and the second-order split-operator method, we calculated the Auger election wave function from Eq. (1) numerically using the generalized pseudospectral method in the energy representation [15]. The single-electron wave functions of the occupied orbitals in $|\Psi_h(N-1)\rangle$ and $|\Psi_c(N-2)\rangle$ are calculated from the density functional theory with the self-interaction-correction method [16].

To speed up the convergence of the simulation, we added a temporal window function $e^{-\tau^2/T^2}$ in Eq. (1). Thus, after a long propagation time we can expand ψ_a as

$$\psi_a(\mathbf{r},t\to\infty) = \int C(\epsilon)\psi_\epsilon(\mathbf{r})\,d\epsilon, \quad (8)$$

where $\psi_\epsilon(\mathbf{r})$ is the laser-field-free atomic continuum wave function, and ϵ is the Auger electron energy. The energy distribution of the emitted electron is expressed as

$$\frac{dP(\epsilon)}{d\epsilon} = |C(\epsilon)|^2, \quad (9)$$

and the LEAD rate is written as

$$R_a = \frac{\sqrt{2\pi}}{T}\int_0^{\infty}\frac{dP(\epsilon)}{d\epsilon}d\epsilon. \quad (10)$$

The $\sqrt{2\pi}/T$ term is introduced because we added a temporal window function. If there is no IR laser field, Eq. (10) reduces to the standard expression for the Auger decay rate. Due to the energy deficiency, the Auger decay rate goes to zero for a valence ns hole of rare-gas atoms without the IR field. The numerical simulations of the LEAD process are similar to the simulations of the above-threshold ionization (ATI) spectra, and the details can be found in [17,18].

III. THEORETICAL RESULTS AND DISCUSSION

Based on the above method, we calculate the LEAD rates of Xe, Kr, Ar, and Ne rare-gas atoms. In the simulation, we choose an IR pulse with a 40-fs pulse duration [the full width at half maximum (FWHM)], wavelength of 800 nm, and a moderate laser intensity to avoid direct laser ionization of the outer shell electron. The numerical convergence was tested by varying the number of grid points, partial waves, and sphere size. The numerical data presented here were calculated with a sphere radial size of 200 a.u. (a.u. denotes atomic units), 512 grid points, and 32 partial waves.

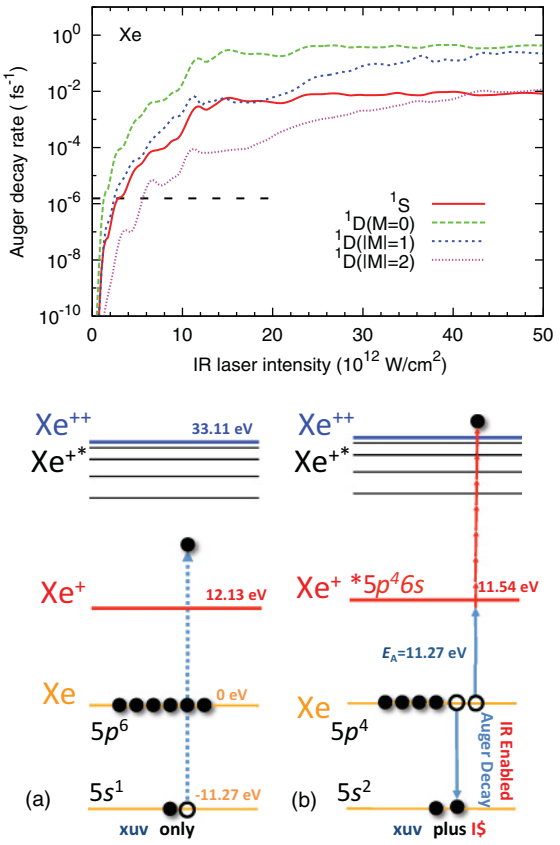

FIG. 2. (Color online) Upper panel: IR-enabled Auger decay rates for Xe, with Xe^{2+} ions in the ^1S state (solid line) and ^1D states (dashed lines). The horizontal dashed line indicates the radiative decay rate of the hole. Lower panel: (a) Xe energy diagram for the lowest single- and double-ionization thresholds with a 5s electron ionized by an XUV pulse. (b) A 5p electron can be ejected to an Xe^{+*} Rydberg orbit or the Xe^{++} continuum through the LEAD process after a respective absorption of at least one or seven IR photons.

Figure 2 (upper panel) shows the LEAD rates of Xe as a function of the IR laser intensity for the doubly ionized ionic core in the ^1S and ^1D states.

To check how the LEAD rates change as a function of the propagation time, we also calculated the decay rates of the ^1D state with $M = 0$, for an 80-fs FWHM temporal function. The decay rates do not depend on the propagation time. At lower IR laser intensities($<10^{12}$ W/cm^2), the LEAD rates are negligibly small. The rates increase dramatically when the IR intensity increases to $4I_0$ with $I_0 = 10^{12}$ W/cm^2. For $M = 0$ states, the rates reach peak values for the laser intensity of $11I_0$, and then decrease slowly. By analyzing the energy structures of Xe ions with a 5s hole as shown in Fig. 2 (lower panel), we find that the 6s orbital energy is close to the energy difference of E_h and E_c. Thus, in the presence of the IR laser field, the 5s hole can be filled by one of the 5p electrons, while another 5p electron is excited to the Xe^{+*} Rydberg states temporally. Figure 2 (lower panel) shows that the 6s orbital is the lowest possible Rydberg state, and it can be easily ionized by the IR laser with the absorption of at least seven IR photons.

Note that the LEAD rate depends on the energy defect, and that the IR intensity also increases this defect through

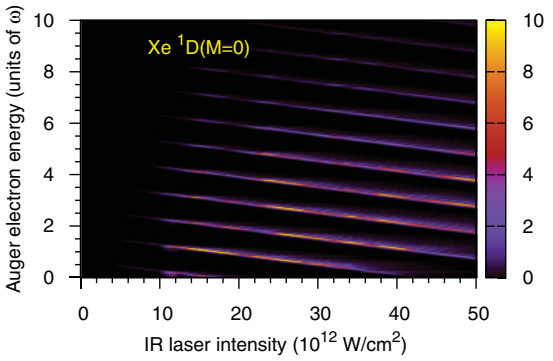

FIG. 3. (Color online) Energy distribution of the Auger electron as a function of the IR laser intensity for Xe, with the Xe^{2+} ions in the $^1D(M = 0)$ state.

the ponderomotive shift of the atomic energy levels [19,20]. Thus, as the IR laser intensity increases, the LEAD rates may decrease slowly, as shown in Fig. 2 (upper panel). This ponderomotive effect can be seen more clearly in the energy spectra of the Auger electrons as shown in Fig. 3. The Auger electron spectra are similar to the ATI spectra of atoms in a laser field [21–23], with sharp peaks separated by one IR photon energy. Below the IR laser intensity of $20I_0$, the IR laser can doubly ionize Xe by adding at least seven IR photons to the Auger 5p electron. As the intensity increases above $20I_0$, the IR laser can doubly ionize Xe by adding at least eight IR photons to the Auger electron, thus decreasing the decay rates.

LEAD is a general laser-enabled process and it should also occur in other rare-gas atoms. Figures 4 shows the LEAD rates for Kr, Ar, and Ne. Different from the Xe case, we present the LEAD rates for the ^1S and ^1D states without the detail distribution of the M sublevels. In these gases, the general trend of the LEAD rates as a function of the IR laser intensity is similar to that in Xe. For Kr and Ar, the leading decay channel is the ^1D state, similar to Xe. We see that the relative contribution of the ^1S state increases in the Kr and Ar targets. On the other hand, the leading decay channel in Ne is ^1S, while the contribution from the ^1D channel is much smaller.

These results can be explained in terms of the relevant atomic energy structures. The energy defects of the ns hole to the double-ionization threshold calculated by the method described in Ref. [16] are 18.56, 14.08, 10.90, and 9.80 eV for Ne, Ar, Kr, and Xe, respectively. The IR laser field can easily induce the Auger decay for a small energy defect, namely, for Xe and Kr. This explains why we need a high IR laser intensity to induce the LEAD process in the case of Ne.

To explain the differences in the contributions of the final doubly charged states for different targets, we intuitively analyze the overlap of the outgoing partial waves and the relevant electronic structures of Ne, Ar, Kr, and Xe. The precursor state (3d) of a d partial wave has a very small overlap with the inner-valence 2s and 2p orbitals in Ne, and therefore the contribution from the s-channel is dominant. In the case of Xe, the 4d orbital is an occupied orbital and the overlap of the d states with the 5s and 5p orbitals is larger than the overlap of the s states. This results in a larger contribution from the ^1D states, compared with the Kr case. For Ar, the 3d orbital

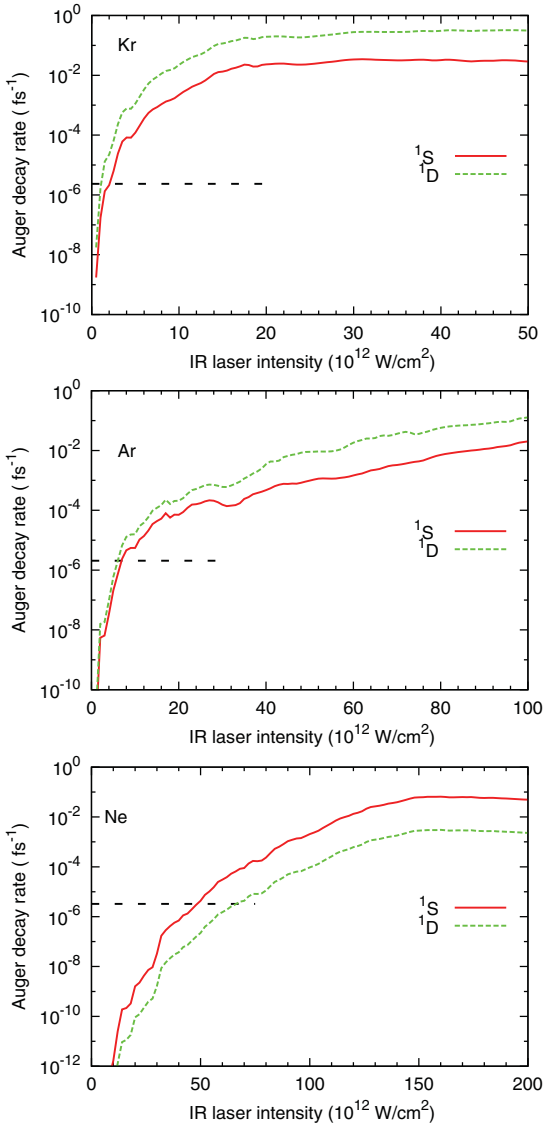

FIG. 4. (Color online) IR-enabled Auger decay rates for Kr, Ar, and Ne to ^1S and ^1D. The horizontal dashed lines indicate the radiative decay rates of the holes.

is not occupied but has a large overlap with the inner-valence orbitals $3s$ and $3p$. This nicely explains why the d channel contributes more than the s channel for Ar, Kr, and Xe.

IV. EXPERIMENTAL RESULTS AND DISCUSSION

To find evidence of LEAD processes, we performed experiments on the double ionization of Ar and Xe atoms using time-resolved femtosecond IR and 36-eV XUV pulses in a cold target recoil ion momentum spectroscopy (COLTRIMS) geometry. For Ar, 36 eV is well below the double-ionization threshold, and several possible DI channels open up in the presence of an IR pulse as intense as 7×10^{12} W/cm^2 [12]. For Xe, the 36 eV photon energy is just above the DI threshold and the number of DI channels significantly reduces compared with the Ar case. For example, Xe** ($5p^4$) and Xe^{+*} ($5p^5$) states are not possible, as was the case in Ar. In Xe, a 36 eV XUV photon can create a $5s$ hole and leave the singly charged Xe in the ground state after a $5p$-$5s$ radiative relaxation, or leave $5s$ Xe in a highly excited state [Fig. 2 (lower panel)]. In the former case, the IR pulse can ionize Xe$^+$ through the LEAD process with rates several orders of magnitude larger than the radiative $5p$-$5s$ decay [Fig. 2 (upper panel)]. The ability to enable Auger decay with rates significantly higher than radiative decay opens up possibilities for controlling electron-electron interactions in atoms and molecules.

Our experimental setup consists of a high-power (30 W), high repetition rate (10 kHz) 30-fs Ti:sapphire laser system (785 nm), a gas-filled waveguide for generating harmonics, and a COLTRIMS apparatus which allows the simultaneous detection of ion and electron three-dimensional momenta. Using part of the laser output, high harmonics are generated in Ar gas and then refocused into separate Ar and Xe supersonic gas jets using a pair of multilayer XUV mirrors which reflect photon energies around 36 eV. A 200-nm thick Al filter is inserted in the XUV beam to attenuate the driving IR pulses reflected from the XUV mirrors. Even a weak IR laser beam copropagating with the XUV beam can damage the XUV coating. This results in higher reflectivity of lower harmonics. In this case, the 13th and 15th harmonics are reflected from the XUV optics as seen in the Ar photoelectron spectrum shown in Fig. 5 (lower panel). Another part of the laser beam is temporally and spatially recombined with the XUV beam in a collinear fashion, and focused onto the Xe and Ar targets at a laser intensity of 7×10^{12} W/cm^2. A linear stage, with 260-as resolution, was used to delay the IR pulse relative to the XUV pulse. The XUV pulse duration was approximately 10 fs.

Figure 5, upper and lower panels, respectively, shows the Ar DI yield as well as the ratios of Ar^{++}/Ar$^+$ yields, and a photoelectron yield, taken in coincidence with Ar$^+$ atoms,

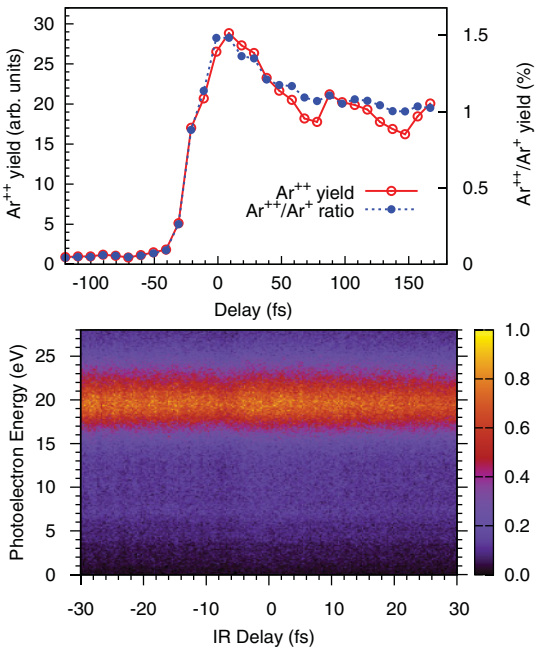

FIG. 5. (Color online) Ar^{++} and Ar^{++}/Ar$^+$ yields as a function of the delay between the XUV and IR pulses (upper panel). The photoelectron spectra taken in coincidence with Ar$^+$ ions in the overlap region (lower panel).

as a function of the XUV-IR relative delay. Negative delays represent the case when the IR pulse precedes the XUV pulse, while positive delays present the case when the IR pulse arrives after the XUV pulse. The two pulses overlap temporally for the delays between −30 and +30 fs (overlap region). Figure 5, upper panel, shows that the moderate IR field enhances the Ar^{++} yield by roughly 30 times in the overlap region, while the Ar^{++}/Ar^{+} ratio maximizes at about 1.6%. The photoelectron yield taken in coincidence with Ar^{+} ions (Fig. 5, lower panel) shows a peak around 20 eV corresponding to photoionization of a $3p$ electron by the 36-eV XUV photon. If the XUV pulse ionizes a $3s$ electron (binding energy 29.2 eV), we expect to see a photoelectron signal around 6.2 eV, after subtracting the ponderomotive potential of about 500 meV. The photoelectron yield in that region shows two lines at 4.2 and 7.4 eV, corresponding to a $3p$ electron ionized by the 13th and 15th harmonics "leaking" though the XUV reflective optics. Since the 36-eV XUV photon is 7.5 eV below the double-ionization threshold, the Ar^{++} enhancement in the overlap region could come from coupling of the Ar^{+*} and Ar^{**} $3p$ states into the double-ionization continuum by the IR pulse. Single-photon double ionization is a resonant process and the Ar^{++} yield of IR field ionization of Ar^{**} should be sensitive to the XUV energy. The pattern of the Ar^{++}/Ar^{+} yield obtained by the 36-eV XUV photon is similar to the one obtained by the 42-eV XUV source [12]. Therefore, the additional DI yield enhancement also comes from a LEAD process where the 36-eV photon ionizes a $3s$ electron, while the IR field couples an Auger $3p$ electron to the DI continuum.

Figure 6, upper and lower panels, respectively, shows a Xe double-ionization yield as well as the ratios of Xe^{++}/Xe^{+} yields, and the photoelectron yield, as a function of XUV-IR relative delay. The data was taken by using similar XUV and IR parameters as for the Ar data shown in Fig. 5. By doubly ionizing Xe using a 36-eV XUV pulse, we make sure that the highest double-ionization threshold ($^1D_2$ 35.5 eV) is still below the XUV photon energy. By doing so, we eliminate the DI contribution from the Xe^{+*}/Xe^{**} $5p$ states ionized by the IR pulse. This results in a significantly smaller enhancement of the Xe^{++} yield in the overlap region, compared with the Ar^{++} enhancement (30:1.7 in favor of Ar), and in a higher Xe^{++}/Xe^{+} ratio (4:1.6 in favor of Xe). The flat Xe^{++} yield for positive IR delays shows that short-lived, autoionizing double excited states probably do not play a significant role in this case. From the photoelectron spectra [Fig. 6 (lower panel)], we notice that the lower harmonics (13th and 15th) contribute more significantly to the Xe^{+} yield compared with the Ar case. Thus, the Xe^{++}/Xe^{+} yield coming from the 36-eV photon channel is probably even higher than shown in Fig. 6 (upper panel). In the case of Xe, 7×10^{12} W/cm^2 IR intensity can ionize Xe, as seen at 0.2-eV electron energy at both positive and negative delays in Fig. 6. By setting up the experiment in this way, we make sure that the LEAD process is experimentally possible, since the Xe LEAD deficiency is only 9.80 eV. However, even though we were able to decrease the number of the IR-enabled double-ionization channels by using an XUV photon energy just above the DI threshold, isolating unambiguously the LEAD process remains an experimental challenge.

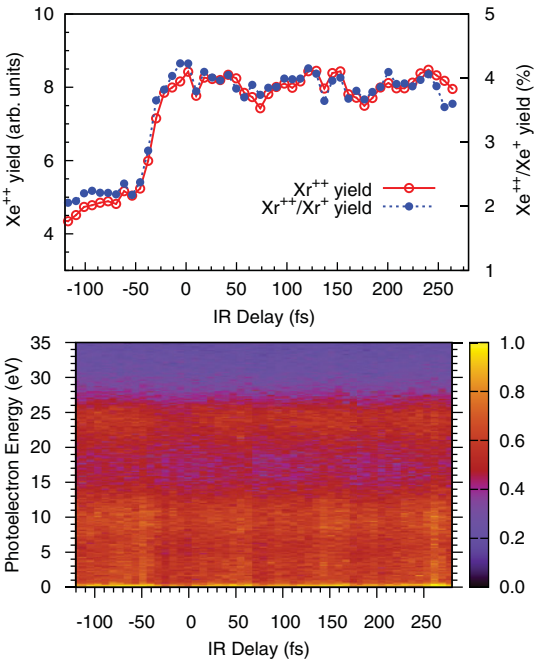

FIG. 6. (Color online) Xe^{++} and Xe^{++}/Xe^{+} yields as a function of the delay between the XUV and IR pulses (upper panel). Photoelectron spectra taken simultaneously with the Xe ions (lower panel).

In addition to exploring femtosecond delays, we performed a time-resolved experiment with attosecond resolution in the overlap region. Figure 7 shows the Xe^{++} versus Xe^{+} yield as a function of the XUV-IR delays. In this experiment, in addition to the 36-eV XUV harmonic we allow the lower harmonics (lower than the Xe ionization potential) to populate neutral Xe^{*} states. We did this by taking the Al filter out of the XUV beam. By doing this, we lock a weak IR pulse (3×10^{11} W/cm^2) to the XUV pulse in the time domain, and let both beams copropagate. The inset of Fig. 7 shows the XUV and IR

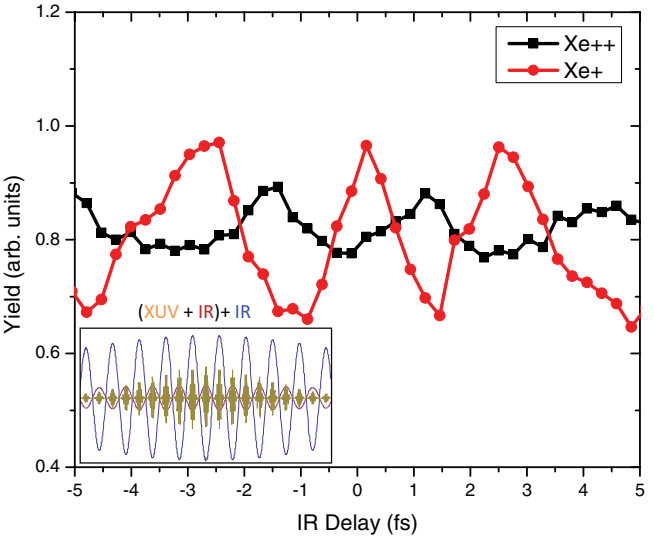

FIG. 7. (Color online) Xe^{+} and Xe^{++} yields as a function of the XUV-IR pump and IR probe pulses. The XUV and IR pulses in the time domain are shown in the inset.

pulses in the time domain. As we delay the probe IR beam (7×10^{12} W/cm^2) on an attosecond time scale relative to the XUV-IR pump beam, we change the total intensity the atom sees at the instant of the strobe XUV pulse [24,25]. By doing so we control the Xe^{++}/Xe^{+} yields both by modulating the total IR intensity and by interfering the electron wave packets. The phase difference of about a half optical cycle is telling us that different processes are responsible for the coherent control of the single- and double-ionization Xe yields. The interference of the two electronic wave packets with the final energy of the 8th harmonic (7th+IR and 9th-IR) are responsible for the modulation of the Xe^{+} yield, while the modulation of the Xe^{++} yield can occur through several different channels. The LEAD channel is very sensitive to the IR intensity as shown in Fig. 2, but also it is possible that the phase of the XUV and IR pulses plays a role. Thus, we are not surprised that the Xe^{+} and Xe^{++} yields get modulated at different phases, and with different amplitudes. To compare our calculations with this experiment and to gain insight into the physical processes, we need to convolve the time-dependent Auger electron wave function in Eq. (1) with the time-dependent photoelectron wave function of the ns orbital ionized by the XUV pulse in the presence of the IR field. In this way we can retain the history of the creation of the ns hole and also the phase information. We expect that the LEAD process would depend on the time delay between the attosecond XUV pulse (creation of the hole) and the probing IR field (induced Auger decay). Thus we can both induce Auger decay by employing an IR laser field and control the process by tuning the time delay between the two pulses.

V. SCREENING EFFECTS

Comparing the calculated LEAD rates with the experimental observation for Xe atoms, we found that the decay rates are on the order of 10^{-2} fs^{-1} at the applied IR intensity. Therefore, once a $5s$ hole is created, it can easily decay through the LEAD process when the IR laser is applied. For Ar atoms, the LEAD rates are on the order of 10^{-5} fs^{-1} at the applied IR intensity. So the contribution from the LEAD should be negligible. This contradicts the LEAD explanation of our experimental observations. Where is the problem?

So far, we focused our attention on the general phenomena of laser-enabled Auger decay, assuming that the subvalence ns hole has been created before applying the IR field and that the ns hole has no phase relation with the probe (enabling) IR laser. We have also ignored the screening effect due to the spectator photoelectron, which in general reduces the energy defect. If the XUV and IR pulses arrive simultaneously, the photoelectron is still in the vicinity of the parent ionic core when the IR-enabled Auger decay happens. The presence of the spectator photoelectron reduces the energy defect, which increases the LEAD rate significantly. The outer-screening effect can be taken into account by replacing the electron-nuclear Coulomb interaction with a Debye screening potential as

$$V_c(r) = -\frac{Z}{r} \;\rightarrow\; V(r) = -\frac{Z}{r}e^{-r/\lambda_d}, \tag{11}$$

where Z is the atomic number and λ_d is the Debye length. Using the density functional theory with the self-interaction-correction method [15], we obtain the energy defect and the effective potential. With the effective potential, we can calculate the orbital wave functions and the LEAD rates. The Debye length can be estimated by replacing the temperature with the kinetic energy of the photoelectron and by using the density as $3(vt)^{-3}/4\pi$ with v the velocity of the photoelectron and t the time after the creation of the hole. With these assumptions, the Debye length can be expressed as

$$\lambda_d = \sqrt{3v^5t^3/2}. \tag{12}$$

From the present experiment conditions, Debye screening effect lasts for an order of 10 fs.

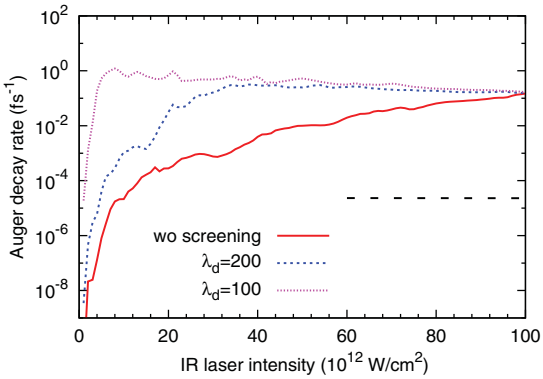

FIG. 8. (Color online) Total IR-enabled Auger decay rates of Ar atoms for different Debye lengths.

Taking the Ar atom as an example, the energy defect reduces from 14.1 eV (without screening) to 13.2 (for $\lambda_d = 500$ a.u.), 11.8 (for $\lambda_d = 200$ a.u.), and 9.4 eV (for $\lambda_d = 100$ a.u.). The total LEAD rates with the screening effect are plotted in Fig. 8. Overall, we see that the screening effect increases the LEAD rates greatly for the lower IR intensities, and the rates reach saturation quickly for $\lambda_d = 100$ a.u., corresponding to a strong screening case. For a weak screening case, $\lambda_d = 200$ a.u., the LEAD rate decreases. This explains why the DI yield maximizes in the overlap region between the IR and XUV pulses then decreases as the time delay increases for Ar. For Xe, the additional yield enhancement in the overlap region is absent. At the IR laser intensity used in the experiment, we expect the LEAD Xe^{++} yield enhancement to be saturated due to the smaller energy deficiency, thus making no difference whether the XUV and IR pulses are temporally overlapped, or the IR pulse arrives after the XUV pulse.

As we discussed above, LEAD processes can be further classified into two types: a resonant LEAD process in which there is one dominant bound state involved as an intermediate state and a nonresonant LEAD process in which there is no such dominant bound state. For the resonant LEAD process, the LEAD rate strongly depends on the energy structure of the atomic ions or the model potential used in the simulation. Figure 9 shows the total LEAD rates calculated using two different model potentials. One is a six-parameter model potential [13] and the other is a three-parameter potential [26] as $V(r) = -[2 + ae^{-br} + (16 - a)e^{-cr}]/r$ with $a = 8.9$, $b = 1.5$, $c = 6.1$. The parameters are obtained by fitting the numerical potential of Ar^{+} from density functional theory [16]. The general

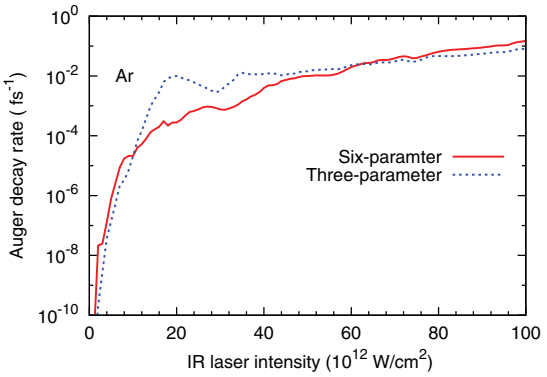

FIG. 9. (Color online) Total IR-enabled Auger decay rates of Ar atoms calculated from different model potentials.

trends of the LEAD rates obtained from the two model potentials are close to each other. A large discrepancy appears at 2×10^{13} W/cm^2. By analyzing the energy spectra of the Auger electron, we attribute the discrepancy to a resonant LEAD process. The quantitative differences predicted by different model potentials do not change the physical conclusion of this study.

Note that a similar Xe experiment was reported by Guyetand *et al*. [27]. The data shown there, even though lacking in statistics, are an example of a state-of-the-art COLTRIMS experiment, and already showed the LEAD double-ionization channel. From Fig. 2, it is obvious that LEAD double ionization would produce two electrons that share the energy unequally. The first electron is ionized from the 5*s* subshell by the XUV photon and carries a discreet energy, while the second electron emerges with low kinetic energies in the form of ATI peaks (Fig. 3). In this case even the electron angular distributions are different. The XUV electron angular distribution should have signature of a *p* partial wave, while the second, a LEAD *p* electron absorbs seven additional IR photons. The authors observed this channel and noticed the nonlinear sharing (region 4 in Fig. 14 of Ref. [27]) but did not consider a possibility of explaining the channel through LEAD process.

VI. SUMMARY

We developed a general theoretical method for calculating LEAD yields and applied it to rare-gas atoms. We showed that the presence of a moderate IR field can turn on an Auger decay of an *ns* subvalence shell with rates several orders of magnitude higher than the radiative decay through which an atom naturally relaxes without the presence of an IR laser field. We discussed how screening of an outgoing *ns* electron can increase the LEAD yield when the XUV and IR pulses overlap in time. By doing two-color XUV-IR attosecond and femtosecond time-resolved experiments in Xe and Ar, we separated several different IR-induced double-ionization channels and discussed ways of controlling Auger decay processes. In future work, we will focus on the coherent control processes and attosecond electron-electron dynamics in atomic and molecular targets.

ACKNOWLEDGMENTS

This research was supported by a Grand-in-Aid for Scientific Research (C), from the Japan Society for the Promotion of Science, and by the U.S. National Science Foundation. We thank Achim Czasch, Till Jahnke, and RoentDek for the COLTRIMS support, and Yanwei Liu, Farhad Salmassi, and Eric Gullikson of LBNL for their help with the XUV mirror coatings.

[1] T. E. Glover, R. W. Schoenlein, A. H. Chin, and C. V. Shank, Phys. Rev. Lett. **76**, 2468 (1996).
[2] L. Miaja-Avila, C. Lei, M. Aeschlimann, J. L. Gland, M. M. Murnane, H. C. Kapteyn, and G. Saathoff, Phys. Rev. Lett. **97**, 113604 (2006).
[3] H. Aksela and S. Aksela, Rev. Phys. Chem. **76**, 370 (2007).
[4] M. Drescher, M. Hentschel, R. Kienberger, M. Uiberacker, V. Yakovlev, A. Scrinizi, T. Westerwalbesloh, U. Kleineberg, U. Heinzmann, and F. Krausz, Nature (London) **419**, 803 (2002).
[5] T. Mercouris, Y. Komninos, and C. A. Nicolaides, Phys. Rev. A **76**, 033417 (2007).
[6] C.-H. Zhang and U. Thumm, Phys. Rev. A **80**, 032902 (2009).
[7] C. Buth and K. J. Schafer, Phys. Rev. A **80**, 033410 (2009).
[8] A. K. Kazansky, I. P. Sazhina, and N. M. Kabachnik, J. Phys. B **42**, 245601 (2009).
[9] Y.-C. Chiang, P. V. Demekhin, A. I. Kuleff, S. Scheit, and L. S. Cederbaum, Phys. Rev. A **81**, 032511 (2010).
[10] T. Shimizu, T. Sekikawa, T. Kanai, S. Watanabe, and M. Itoh, Phys. Rev. Lett. **91**, 017401 (2003).
[11] L. Miaja-Avila, G. Saathoff, S. Mathias, J. Yin, C. La-o-vorakiat, M. Bauer, M. Aeschlimann, M. M. Murnane, and H. C. Kapteyn, Phys. Rev. Lett. **101**, 046101 (2008).
[12] P. Ranitovic, X. M. Tong, C. W. Hogle, X. Zhou, Y. Liu, N. Toshima, M. M. Murnane, and H. C. Kapteyn, Phys. Rev. Lett. **106**, 053002 (2011).
[13] X. M. Tong and C. D. Lin, J. Phys. B **38**, 2593 (2005).
[14] R. D. Cowan, *The Theory of Atomic Structure and Spectra* (University of California, Berkeley, 1981).
[15] X. M. Tong and S. I. Chu, Chem. Phys. **217**, 119 (1997).
[16] X. M. Tong and S. I. Chu, Phys. Rev. A **55**, 3406 (1997).
[17] X. M. Tong, K. Hino, and N. Toshima, Phys. Rev. A **74**, 031405 (2006).
[18] X. M. Tong, S. Watahiki, K. Hino, and N. Toshima, Phys. Rev. Lett. **99**, 093001 (2007).
[19] M. D. Davidson, J. Wals, H. G. Muller, and H. B. van Linden van den Heuvell, Phys. Rev. Lett. **71**, 2192 (1993).
[20] E. S. Toma, H. G. Muller, P. M. Paul, P. Breger, M. Cheret, P. Agostini, C. Le Blanc, G. Mullot, and G. Cheriaux, Phys. Rev. A **62**, 061801 (2000).
[21] S. I. Chu and J. Cooper, Phys. Rev. A **32**, 2769 (1985).

[22] R. R. Freeman, P. H. Bucksbaum, H. Milchberg, S. Darack, D. Schumacher, and M. E. Geusic, Phys. Rev. Lett. **59**, 1092 (1987).
[23] P. B. Corkum, N. H. Burnett, and F. Brunel, Phys. Rev. Lett. **62**, 1259 (1989).
[24] P. Ranitovic *et al.*, New J. Phys. **12**, 013008 (2010).
[25] P. Ranitovic, X. M. Tong, C. W. Hogle, X. Zhou, Y. Liu, N. Toshima, M. M. Murnane, and H. C. Kapteyn, Phys. Rev. Lett. **106**, 193008 (2011).
[26] H. G. Muller and F. C. Kooiman, Phys. Rev. Lett. **81**, 1207 (1998).
[27] O. Guyetand *et al.*, J. Phys. B **41**, 065601 (2008).